Nonlinear Terahertz Generation: Chiral and Achiral Meta-atom Coupling

Qingwei Wang, Xueqian Zhang, Quan Xu, Xi Feng, Yongchang Lu, Li Niu, Xieyu Chen, Eric Plum, Jianqiang Gu, Quanlong Yang, Ming Fang, Zhixiang Huang, Shuang Zhang, Jiaguang Han*, Weili Zhang**

Q. Wang, X. Zhang, Q. Xu, X. Feng, Y. Lu, L. Niu, X. Chen, J. Gu, J. Han
Center for Terahertz Waves and College of Precision Instrument and Optoelectronics Engineering, and the Key Laboratory of Optoelectronics Information and Technology, Tianjin University
Tianjin 300072, People's Republic of China
E-mail: alearn1988@tju.edu.cn, jiaghan@tju.edu.cn

E.Plum
Optoelectronics Research Centre and Centre for Photonic Metamaterials, University of Southampton
Highfield, Southampton SO17 1BJ, UK

Q. Yang
School of Physics and Electronics, Central South University
Changsha 410083, Hunan, People's Republic of China

M. Fang, Z. Huang
Key Laboratory of Intelligent Computing and Signal Processing, Ministry of Education, Anhui University
Hefei 230039, People's Republic of China

S. Zhang
Department of Physics, Faculty of Science, University of Hong Kong
Hong Kong 999077, People's Republic of China

J. Han
Guangxi Key Laboratory of Optoelectronic Information Processing, School of Optoelectronic Engineering, Guilin University of Electronic Technology, Guilin 541004, China

W. Zhang
School of Electrical and Computer Engineering, Oklahoma State University
Stillwater, Oklahoma 74078, USA
E-mail: weili.zhang@okstate.edu

Keywords: nonlinear metasurface, coupling, broadband terahertz generation, amplitude tuning, nonlinear circular dichroism

Abstract

Generation and manipulation of terahertz (THz) waves are of vital importance to advance THz technology. Nonlinear metasurfaces allow effective integration of both processes into a single compact device. However, such existing THz devices commonly rely on utilizing a single meta-atom, which has fixed THz generation property and thus limits the range of achievable functionalities. Here, for the first time to our knowledge, we introduce coupling effect between different meta-atoms into the unit-cell design, and experimentally validate this new degree of freedom in controlling the nonlinear THz generation, where achiral coupling provides full control over the amplitude of the generated THz field, while chiral coupling makes the THz generation sensitive to the handedness of the pump polarization. In particular, the chiral coupling case further allows a multiplexing-based handedness-selective nonlinear metasurface, which generates THz beams with different orbital angular momentums (OAMs). This approach is promising in developing various integrated nonlinear THz devices.

1. Introduction

Terahertz (THz) waves are a frontier for ultra-high-speed communication,[1,2] biologic sensing,[3] and security imaging technologies.[4,5] The development of these fields relies on advances in THz generation, manipulation and detection. Conventionally, these processes are performed separately by different components in space. This provides flexibility in composing various applications through combining components with different available functionalities, but prevents the construction of compact systems. Integration of multiple processes into a single device provides one effective way to overcome the above problem. Here, we take the THz generation and manipulation processes as examples. Conventional THz sources include photoconductive antennas,[6] nonlinear crystals,[7] air plasma,[8] and spintronic emitters,[9-12] etc. However, on the condition of not modulating the pump lasers, they all lack flexibilities in further controlling the propagation properties of the generated THz waves at the same time, such as the amplitude, phase, wavefront and pump polarization dependence. As for THz manipulators, they have undergone a rapid development in recent years benefitting from the metasurface method, such as chiral-related devices,[13-15] deflectors,[16-18] special beam generators,[19,20] holograms,[21,22] and active spatial THz modulators,[23,24] etc. However, they can only manipulate existing THz waves owing to their linear working feature, which will also bring additional insertion loss and bandwidth limits when putting them into the THz paths.

Recently, nonlinear metasurfaces have attracted growing interest,[25,26] and emerged as an promising route in combining both the THz generation and manipulation processes. The THz generation functionality is arisen from their nonlinear working feature, i.e., the difference frequency generation (DFG) process under femtosecond laser pump,[27] while the simultaneous manipulation functionality is originated from the engineerable feature of the constituent structures, which can serve as an effective way in designing the phase, polarization and wavefront of the generated THz waves.[28-30] Resonating in the infrared regime, the structures in nonlinear metasurfaces are commonly in a nanoscale feature size, which implies an extremely

high local controlling resolution (≈λ/500) and also miniaturized footprint for manipulating THz field. Compared with their linear metasurface counterparts composed of structures of hundred-micro scale, the controlling resolution is about two orders of magnitude improved.

Thus far, several different types of such nonlinear metasurfaces have been reported, which are commonly based on split-ring resonator (SRR) and C3 (three-fold rotational symmetry) structure.[28-30] SRR is a kind of widely applied meta-atoms in both linear and nonlinear metasurface regimes. For nonlinear applications, SRR is found to be mainly sensitive to the pump polarization components perpendicular to its arms, which generates THz waves with polarization parallel to the arms.[27] C3 meta-atom has a special symmetry, which can only generate THz waves through the DFG process between different circularly polarized pumps.[28] Both of them support nonlinear Pancharatnam–Berry (PB) phase control or associated binary phase control over the generated THz waves through rotating the meta-atoms, thus allowing to further design the THz propagations, such as spatiotemporal angle control and polarization generation,[28,30] beam focusing,[31] as well as vortex beam and toroidal pulse generations.[32]

However, all the above studies are mainly focusing on utilizing single plasmonic meta-atom to control the THz generation. Owing to its fixed geometry, the corresponding nonlinear THz generation property is settled accordingly, which limits the available functionalities to a large extent. Changing the meta-atom's geometry is one effective route to extend the control at the unit cell level, however, it enhances the complexity in engineering the nonlinear processes where repetitious and time-consuming nonlinear simulations are typically required. Coupling effect among adjacent resonators provides a way to overcome the above difficulty. In linear metasurfaces, it has led to many fascinating optical functionalities, such as electromagnetically induced transparency (EIT),[33-35] PT symmetry breaking,[36,37] and resonance splitting,[38-40] etc, where one unique feature of coupling is the fact that it allows tailoring the electromagnetic response without having to modify the geometries of the coupled meta-atoms. Transforming

such a feature into nonlinear metasurfaces, it means one can tune the meta-atom's known nonlinearity though coupling so as to achieve extended functionalities.

In this article, for the first time to our knowledge, we introduce classic EIT coupling into the control of nonlinear THz generation and manipulation upon infrared pump. The basic unit—meta-molecule—is composed of one bright meta-atom and one/two dark meta-atoms. To show the versatile controlling abilities of coupling effect, two types of meta-molecules are experimentally demonstrated, including achiral meta-molecules that provide control over the amplitude of THz emission, and chiral meta-molecules that are sensitive to the handedness of the pump polarization. Besides, a handedness-selective nonlinear THz spin-orbital interaction device is further demonstrated though multiplexing certain mutually enantiomorphous chiral meta-molecules, which can generate broadband THz beam with different orbital angular momentums (OAMs) under different circularly polarized infrared pumps. The proposed approach provides an avenue towards various highly integrated THz generation devices with multiple tailorable functionalities.

2. Results

2.1. Basic controlling strategy

The bright and dark meta-atoms in the designed meta-molecule here are bar resonator and SRR, respectively, as illustrated in **Figure 1**a. According to the symmetry selection rule of second-order nonlinear effect, the bar resonator and its electric dipole resonance can only support out-of-phase nonlinear currents that do not contribute to far-field THz radiation, thus the THz emission here is solely arisen from the magnetic dipole resonance (MDR) of the SRR,[27] whose resonance strengths determines the actual nonlinear effect. In general, MDR in metasurfaces can be excited through two routes, as shown in Figure 1a. One is direct excitation by a pump beam with the electric field polarized perpendicular to the SRR's symmetry axis (↔, *x*-polarization). The other is indirect excitation through the coupling field from the electric dipole

resonance of the bar resonator, which disturbs the SRR's symmetry and is excited by pump field parallel to the bar (↕, *y*-polarization), corresponding to the classical EIT analogue effect in metasurfaces.[33]

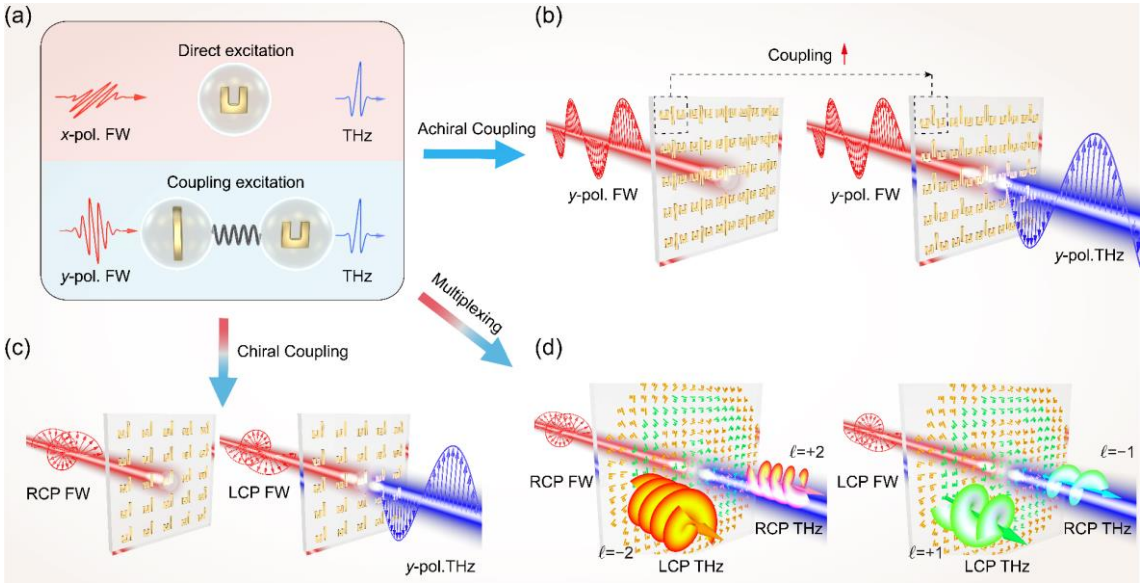

Figure 1. Harnessing coupling to control THz generation. a) Schematic of the two coupling routes of MDR for nonlinear THz generation. b) Coupling-induced THz generation in achiral meta-molecules provides control over the amplitude of the generated THz waves. c) Giant nonlinear circular dichroism of chiral meta-molecules can provide THz generation for circularly polarized pump of only one handedness. d) Handedness-selective nonlinear spin-orbital interaction device composed of left-handed (green) and right-handed (orange) chiral meta-molecules. The generated LCP and RCP THz beams carry orbital angular momentum of $l = -2$ and +2 under RCP FW pump and $l = +1$ and -1 under LCP FW pump.

By tailoring the coupling-enabled indirect excitation using two SRRs in an achiral coupling configuration, the amplitude of the nonlinear THz generation can be effectively tuned under the *y*-polarized pump, as shown in Figure 1b. Whereas by designing the interference between both excitation routes using one SRR to introduce chiral coupling, the nonlinear THz generation can be engineered to be sensitive to the handedness of the circularly polarized pumps, as shown in Figure 1c. Furthermore, in combination with spatial multiplexing and nonlinear PB phase methods, the chiral coupling case with handedness-selective THz

generation ability also allows a multifunctional device that can generate THz vortex beams of OAMs of l = ±1 and l = ±2 under left-handed circularly polarized (LCP) and right-handed circularly polarized (RCP) pumps, respectively, as shown in Figure 1d.

2.2. Achiral coupling for controlling the amplitude of the nonlinear THz generation

According to the nonlinear polarization equation $P_{\mathrm{THz}} = \varepsilon_0 \chi^{(2)}_{\mathrm{THz}} E_1 E_2^*$, the amplitude of the nonlinear THz generation here is determined by the resonance strength of the MDR, where ε_0 is the vacuum permittivity, $\chi^{(2)}_{\mathrm{THz}}$ is the effective 2nd-order nonlinear susceptibility, and E_1 and E_2 are the fundamental wave (FW) fields from the MDR whose frequency difference locates at THz frequencies. In order to excite and enable the control of the MDR, a pair of SRRs are symmetrically placed on the left and right sides of a bar resonator to form an achiral meta-molecule that works for *y*-polarized pump. Their geometric parameters are defined in **Figure 2**a. (For individual resonance properties of the bar resonator and the SRRs, see Figure S1). Under *y*-polarized pump, the field first excites the electric dipole resonance of the bar resonator, which then couples to the SRRs and excites their MDRs (Figure 2b and Figure S2). Even though the MDRs in the two SRRs have a π phase difference, they lead to in-phase nonlinear currents that flow along the arms of both SRRs (Figure 2b) since the phases of E_1 and E_2 cancel with each other in the nonlinear polarization equation, giving rise to the *y*-polarized THz radiation that interferes constructively in the far-field.[27] In this process, stronger coupling strengthens the MDR excitation, which provides a way to tune the amplitude of the nonlinear THz generation by changing the coupling strength. Here, this is achieved via adjusting the position (*y*-separation Δ*S*) of the SRRs relative to the bar resonator.

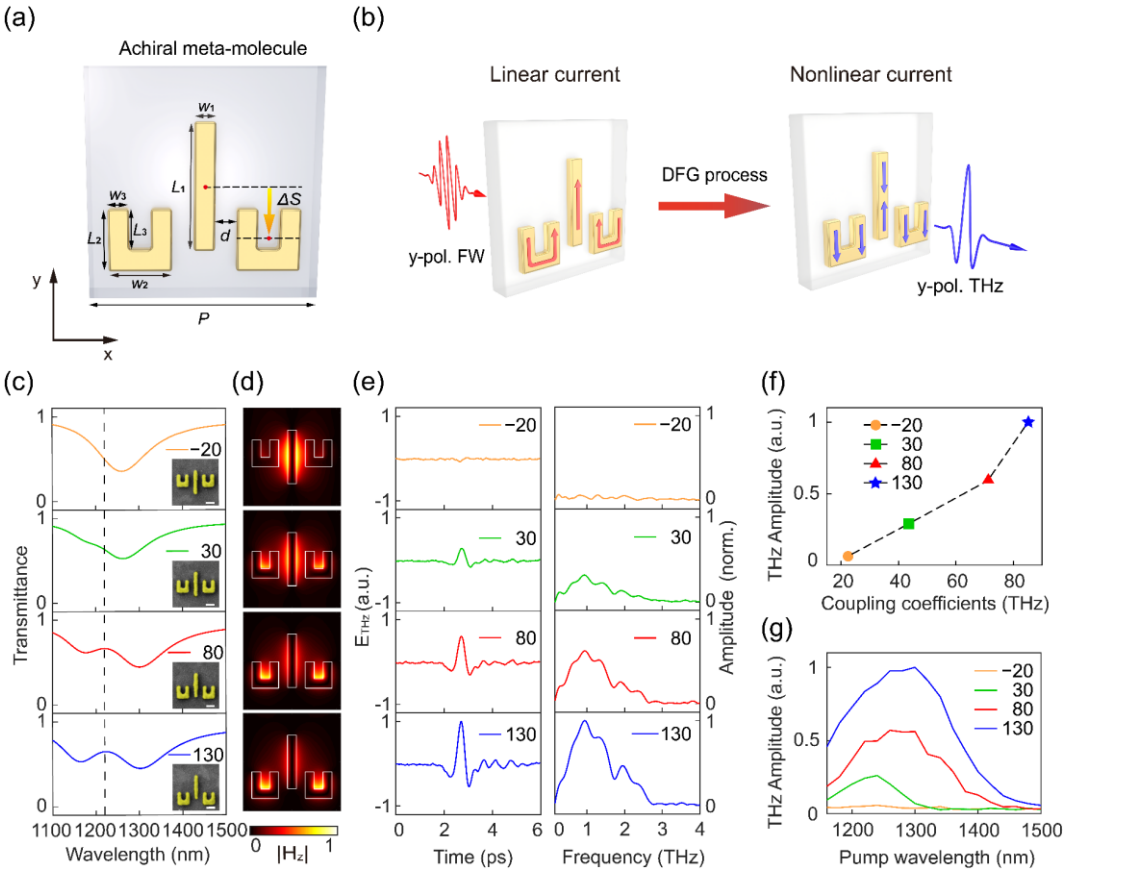

Figure 2. Controlling the amplitude of THz generation through coupling with achiral meta-molecules. a) Schematic of the achiral meta-molecule with geometrical parameters of L_1 = 300 nm, W_1 = 50 nm, L_2 = 150 nm, W_2 = 150 nm, L_3 = 90 nm, W_3 = 50 nm, d = 50 nm, P = 550 nm. ΔS is defined as the displacement of the centers of the SRRs to that of the bar resonator along $-y$. b) The basic working mechanisms of the achiral meta-molecules under the y-polarized illumination. Red and blue arrows represent the linear (FW) and nonlinear (THz) surface current distributions. c) Measured linear transmission spectra of the fabricated nonlinear metasurfaces with ΔS = −20, 30, 80 and 130 nm and corresponding SEM images (scale bar: 100 nm). d) Corresponding simulated H_z-field distributions for y-polarized illumination with 1220 nm wavelength. e) Measured time-domain THz pulses and their Fourier transform under 1220 nm FW pump. f) Extracted THz peak-to-peak amplitudes in (e) as a function of the coupling coefficient κ retrieved from coupled-mode theory. g) Measured THz peak-to-peak amplitude as a function of the FW wavelength under the y-polarized pump.

To demonstrate the above amplitude-tuning strategy, four samples with different ΔS's are fabricated using e-beam lithography (see Experimental Section). Scanning electron microscopy (SEM) images of the meta-molecules are shown as insets of Figure 2c. Figure 2c shows the

measured linear transmission spectra of them under *y*-polarized illumination (see Experimental Section). When ΔS = −20 nm, only a single broad resonance at 1280 nm occurs. As ΔS increases, an EIT window gradually emerges and becomes more pronounced at ≈1220 nm, as indicated by the dashed line in Figure 2c. The relatively broad and weak EIT window here can be attributed to the large Ohmic loss effect in the real metal (see Figure S3). To quantify the variation of the coupling strength, coupled-mode theory is used to fit the measured transmission spectra, revealing that the coupling coefficient increases monotonically with ΔS (Supplementary Section S1 and Figure S4). This dependence results from the interplay between the electric and magnetic coupling of bar resonator and SRRs, which changes from destructive to constructive interference as ΔS increases in the studied range.[41] This trend is also confirmed using numerical simulation, where the MDR at 1220 nm gradually becomes stronger as ΔS increases, as illustrated by the H_z-field distributions in Figure 2d (Supplementary Section S2 and Figure S5). It is thus expected that the amplitude of the nonlinear THz generation will increase accordingly.

To experimentally characterize the nonlinear performance, the samples are measured using a home-build time-domain nonlinear THz emission detecting system (see Experimental Section). The central wavelength of the incident FW is initially fixed at 1220 nm, and the pulse width is about 65 fs. Single-cycle THz pulses are detected from all samples, as illustrated in Figure 2e, indicating broadband THz emission (bandwidths around 2.7 THz). Figure 2e shows that the amplitude of the THz pulses increases dramatically with the increase of ΔS. At ΔS = −20 nm, the THz signal is almost negligible, since the MDR is hardly excited due to weak coupling. As ΔS increases, the THz signal becomes stronger because of the enhanced coupling strength. A 93.8% modulation depth of the THz peak-to-peak amplitude is observed, which is defined as $(\Delta E_{max} - \Delta E_{min})/\Delta E_{max}$ with ΔE_{max} (ΔE_{min}) representing the measured maximum (minimum) THz peak-to-peak amplitudes of the four samples. The strength of the THz signal ΔE increases monotonically with the retrieved coupling coefficient (Figure 2f). Further

enhancement of the coupling coefficient by increasing ΔS is limited by the localization of the resonance fields.

Next, the nonlinear performance in a broad FW wavelength range from 1160 nm to 1500 nm is investigated with a fixed pump fluence of 127.3 μJ cm^{-2} (Figure 2g). Enhanced THz generation with increasing coupling strength is observed throughout the whole wavelength range. These findings are supported by nonlinear numerical simulations based on a Maxwell-hydrodynamic model[29,42] (Supplementary Section S3 and Figure S6a, S6b). The simulations show that the FW wavelengths of maximum THz generation are close to the EIT window where the MDR excitation becomes strongest. Therefore, the spectral dispersion of the measured THz peak-to-peak amplitude (Figure 2g) closely follows the strength of the MDR rather than the strength of overall resonances of the achiral meta-molecule (see Figure S5 for the calculated $|H_z|^2$ at the SRR's center based on linear simulations at different ΔS). It is also noticed that the measured THz generation peak gradually redshifts as ΔS increases (Figure 2g). This may be attributed to the photoinduced heating of the conduction band electrons in the composite materials of the meta-molecule, which causes redshifts of their plasma frequencies,[43-45] since the localized MDR intensity increases with ΔS. In addition, the THz peak-to-peak amplitudes as a function of the pump fluence are also measured (Figure S7), where the linear dependence clearly demonstrates a second-order nonlinear process of the THz generation.

As for the case of the *x*-polarized pump, the response resembles that of individual SRR. As the MDRs of the two SRRs are excited in phase (Figure S2), they actually form a collectively anti-symmetric resonance field distributions, whose coupling fields to the bar resonators cancel with each other and results in overall extinguished couplings. Therefore, the resonance strengths of the MDRs only have little dependence on ΔS, which cannot be used for amplitude tuning applications, as shown in Figure S8. Besides, the nonlinear performance under circularly polarized pump is also experimentally investigated, as shown in Figure S9. In this case, the MDRs of the two SRRs are determined by the interference between the *x*- and *y*-polarized

contributions. The measured results show a growing amplitude of the THz emission as ΔS increases, but the modulation depth is reduced to 27.2% as compared with the case of *y*-polarized pump. The THz intensity at $\Delta S = -20$ nm is nearly halved (53%) to that at $\Delta S = 130$ nm. All these results are consistent well with the linear simulation predictions.

2.3. Near-field chirality in the achiral meta-molecules

In the previous section, it is confirmed that the MDRs could be excited indirectly and directly by incident *y*- and *x*-polarized pump fields, respectively. When the FW pump field contains both *x*- and *y*-polarized components (E_x and E_y), constructive and destructive interference between the in-phase (excited directly by E_x) and anti-phase (excited through coupling by E_y) magnetic dipole modes can occur in the two SRRs. In this case, the THz generation in each SRR will be determined by the amplitude contrast $r = |E_y/E_x|$ and phase difference $\delta = \angle(E_y/E_x)$ of the incident field components. Under *x*-polarized FW illumination, the excitation of both the left and right MDRs, m_l and m_r, can be described by aE_x, where a is an invariant complex excitation coefficient. Whereas, under the *y*-polarized FW illumination, they can be expressed by $\pm bE_y$, where the complex excitation coefficient b is determined by coupling while opposite signs, + and −, apply to different SRRs. Therefore, under an arbitrarily polarized FW illumination, $m_l = aE_x + bE_y$ and $m_r = aE_x - bE_y$. Thus, when the incident polarization satisfies $|a| = |br|$, the left (right) MDR will not be excited due to destructive interference at $\delta + \phi = \pi$ (0) with $\phi = \angle(b/a)$, while the right (left) MDR excitation will be maximized by constructive interference. In particular, for a circularly polarized pump ($r = 1$ and $\delta = \sigma\pi/2$) and the meta-molecules satisfying $b = ia$, LCP ($\sigma = -1$) pump will only excite the left MDR, while RCP ($\sigma = 1$) pump will only excite the right MDR, providing handedness-selective resonance excitation.

The amplitude relation between a and b depends on the coupling strength and can be adjusted by changing ΔS, while the phase difference between the bright electric and dark

magnetic dipole modes is close to π/2 around the dark resonance determined by the EIT coupling nature (Supplementary Section S1). Simulations show that the condition is satisfied by ΔS = 130 nm at a pump wavelength of 1130 nm (Figure S10). However, it should be noted that the handedness-selective MDR excitation can only be observed in the near-field. In the far-field, there is no chiral response, as the achiral meta-molecule has mirror symmetry. Thus, from the nonlinear point of view, the THz emissions will also be the same under LCP and RCP pump, since the two SRRs exhibit identical nonlinear responses. Nevertheless, this effect provides a route to obtain a far-field nonlinear chiral response by removing one SRR from the achiral meta-molecule, resulting in the chiral meta-molecule. Though coupling that affects *a* will emerge under *x*-polarized pump in this case, the geometry can be adjusted to achieve handedness-selective MDR excitation in the remaining SRR.

2.4. Chiral coupling for controlling the chiral response of the nonlinear THz generation

By removing one SRR as mentioned above, chiral meta-molecules are arrived which derive chiral nonlinear responses from planar chiral[46-49] arrangements of a single SRR positioned on the left (or right) side of a bar resonator (**Figure 3**a). It can be designed to only exhibit THz emission under LCP (or RCP) FW pump. It is convenient to describe such optimized meta-molecules as left-handed (right-handed). The handedness-selective THz generation is schematically illustrated in Figure 3b. Meanwhile, the adjustable coupling provides a route to tune the nonlinear chiral response and even to reverse it by changing ΔS. While this also controls the amplitude of the generated THz radiation under certain a circularly polarized pump, the THz field remains *y*-polarized as the THz generation still arises from the MDR in the SRR. To demonstrate this, three samples with different ΔS were fabricated (SEM images shown as insets of Figure 3c). The measured linear transmission spectra under *y*-polarized illumination are shown in Figure 3c. An observable transmission window only occurs at ΔS = 70 nm around 1250 nm, implying significant coupling between the electric dipole resonance and the MDR.

At ΔS = −30 and 20 nm, only single resonance dips are observed, indicating weak coupling. These transmission features are confirmed by the corresponding simulated transmission spectra (Figure S11a), while the coupling strengths are verified by the corresponding MDR strengths in the simulated H_z-field distributions at 1250 nm (insets of Figure 3c, and Figure S11b). The smaller transmission window as compared with the case of achiral meta-molecule can be attributed to the reduced number of SRRs, which causes smaller suppressing effect to the electric dipole resonance. However, this does not bring too much influence on the MDR strength in the single SRR by the coupling excitation route, since its relative position to the bar resonator is not changed too much. Simulated H_z-field distributions arising from circularly polarized pump at 1250 nm wavelength (Figure 3d) show that the handedness-selectivity of MDR excitation indeed increases as ΔS changes from −30 nm to 70 nm. The model predicts that the design with ΔS = 70 nm comes close to handedness-selective MDR excitation around the EIT wavelength, where only LCP pump excites the MDR of the SRR strongly (Figure S11e), implying pump-handedness-selective nonlinear THz generation.

Figure 3e shows the measured THz intensities (square of the THz peak-to-peak amplitudes) of the three samples under LCP and RCP pump in a FW wavelength range of 1160 nm to 1500 nm at a fixed pump fluence of 127.3 μJ cm^{-2}. The FWs are incident from the back side (substrate side) of the samples. Broadband nonlinear chiral responses are observed, which are in good agreement with the above expectations. The difference between the THz intensities generated by LCP and RCP pump increases with ΔS. To quantify the nonlinear chiral response, the corresponding nonlinear circular dichronism (NLCD) defined by NLCD = $\left(I_{\mathrm{LCP}}^{\mathrm{THz}} - I_{\mathrm{RCP}}^{\mathrm{THz}}\right) / \left(I_{\mathrm{LCP}}^{\mathrm{THz}} + I_{\mathrm{RCP}}^{\mathrm{THz}}\right)$ are calculated, where $I_{\mathrm{LCP(RCP)}}^{\mathrm{THz}}$ is the THz intensity under LCP (RCP) pump. The broadband NLCD is clearly largest for the case of ΔS = 70 nm (Figure 3f), whose maximum approaches 0.9 at ≈1350 nm pump wavelength.

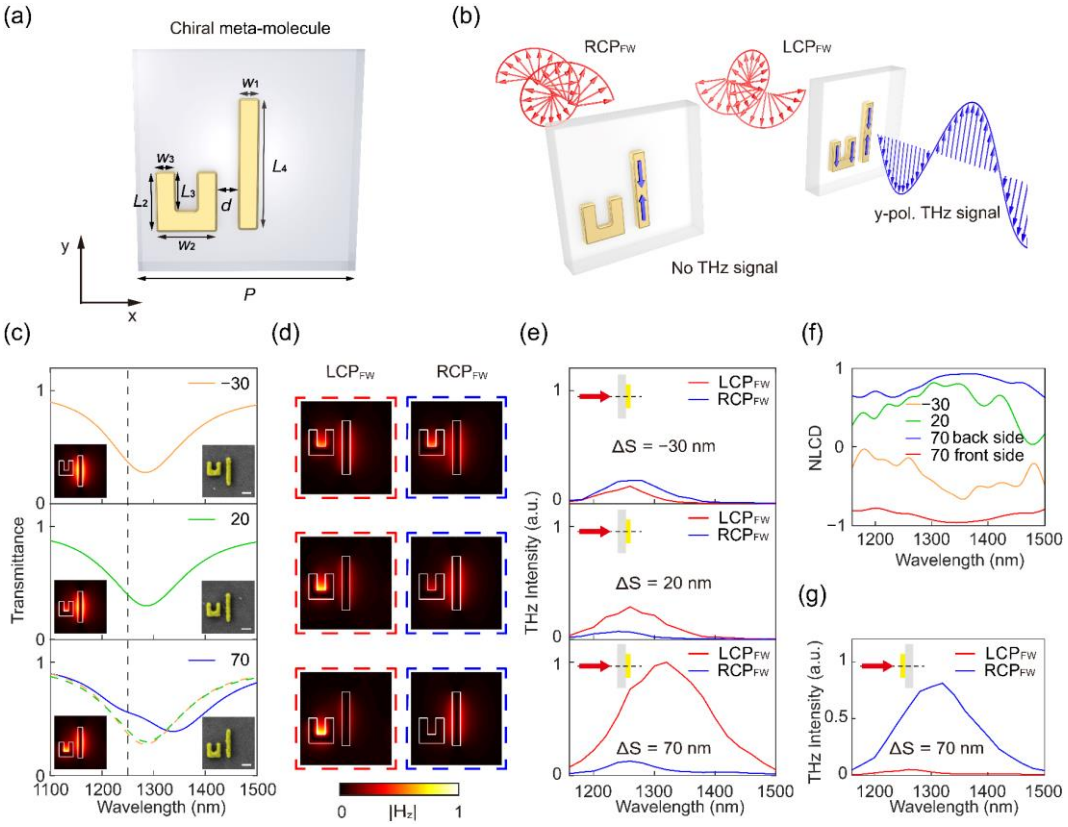

Figure 3. Coupling-controlled nonlinear chiral response in chiral meta-molecules. a) Schematic of the chiral meta-molecule with geometrical parameters, where L_4 = 317 nm and all other dimensions match those of the achiral meta-molecule. b) THz generation by chiral meta-molecules depends on the handedness of the pump. c) Measured linear transmission spectra of the three fabricated metasurfaces with ΔS = −30, 20 and 70 nm under the *y*-polarized illumination and SEM images of the corresponding meta-molecules (scale bar: 100 nm). The color dashed curves in the bottom panel are duplicated results in the top and middle panels for easy comparison. The insets at the left-bottom corners are corresponding simulated H_z-field distributions at 1250 nm wavelength. d) Simulated H_z-field distributions for LCP and RCP pump at 1250 nm wavelength. e) Measured THz intensity as a function of wavelength and handedness of the FW pump that illuminates the back side of the samples. f) NLCD spectra calculated from the results in (e) and (g). g) Measured THz intensity of the sample with ΔS = 70 nm under LCP and RCP FW illumination from the front side, as indicated by the schematic.

For ΔS = −30 and 20 nm, the overall NLCDs have a similar magnitude but opposite signs (Figure 3f). Notably, the reversed chiral response is observed for structures that are not enantiomers. This phenomenon arises from the electric (and magnetic) coupling of bar resonator and SRR (Figure S12). Electric coupling dominates when the SRR is located close to

an end of the bar resonator, where opposite signs of the oscillating charges yield MDR excitation with a π phase difference for SRR placed near opposite bar ends. Thus, the coupling-mediated MDR excitation due to incidence of *y*-polarized electric field E_y changes sign as the SRR is shifted from one bar end to the other, while the direct MDR excitation due to E_x does not change significantly. This switches between constructive and destructive interferences between these contributions to MDR excitation, causing the observed NLCD reversal. To confirm this, nonlinear numerical simulations are also carried out onto the above chiral meta-molecules, where the results agree well with the measurements (Supplementary Section S3 and Figure S6c, S6d).

While NLCD can be reversed by changing ΔS, the simpler and more obvious approach is to reverse the planar chirality of the meta-molecule by moving the SRR from the left of the bar resonator to the right, resulting in the mirror-image chiral meta-molecule (enantiomer). This situation is approximated by illuminating the front (structured side) of the sample instead of its back (substrate side), as shown by the reversed NLCDs (Figure 3f) for illumination from the front (Figure 3g) and back (Figure 3e).

2.5. Handedness-selective nonlinear spin-orbital interaction for THz generation

In contrast to traditional nonlinear optics, nonlinear metasurfaces offer the flexibility to locally engineer amplitude and phase of the generated light. Handedness-selective THz generation provides an opportunity to generate multiplexed THz field distributions by LCP and RCP pump by interleaving left-handed and right-handed meta-molecules. To demonstrate this, a metasurface that generates THz beams with different orbital angular momentum upon LCP and RCP pump is realized (Figure 1d). The device is based on handedness-selective chiral meta-molecules, which are mirror-images of each other, where left-handed (right-handed) meta-molecules are highlighted green (orange). The generated THz radiation is controlled by rotating the meta-molecules, which changes the nonlinear PB phase[29,50] (**Figure 4**a). In a simpler

picture, the polarization of the generated THz wave is linearly polarized and always parallel to the arms of the SRRs. It can be decomposed into RCP and LCP THz components appending with $+\theta$ and $-\theta$ phases for meta-molecule rotation by an angle of $+\theta$. Such nonlinear PB phases are effective as long as the meta-molecule can generate THz radiations, irrespective of the handedness of the incident FW. Our device (Figure 4b) consists of left-handed and right-handed meta-molecules that are rotated clockwise and anticlockwise by $\theta_l = -\varphi$ and $\theta_r = 2\varphi$ and then arranged into ring distributions of different radii, where φ is the azimuth angle. Therefore, the device will generate LCP and RCP THz vortex beams with OAMs of $l = 1$ and -1 under LCP FW pump, while the RCP FW pump will generate LCP and RCP THz vortex beams with OAMs of $l = -2$ and 2.

Figures 4c-f show the measured amplitude and phase distributions of the generated LCP and RCP THz beams under the LCP and RCP FW pump (see Experimental Section). Clear donut-shaped amplitude profiles and vortex phase profiles are observed, which are characteristic for vortex beams. The detected field distributions are the same across the studied spectral range of 0.8 to 1.4 THz, indicating broadband THz vortex beam generation. Owing to the larger divergence of the vortex beams of OAMs of $l = -2$ and 2, they have lower power intensities and thus smaller signal-to-noise ratios as compared with those of $l = 1$ and -1. It should be noted that the RCP and LCP THz beams are generated simultaneously. Their superposition actually forms a linearly polarized vector beam with the local polarization azimuth following the orientation of the SRR arms. Thus, the device could also serve as a pump-handedness-selective vector beam generator. To avoid the superposition, an additional linear phase gradient can be added to the design, which would deflect the circularly polarized THz beams of opposite handedness by opposite angles. Indeed, nearly arbitrary THz Poincaré beams could be generated by designing handedness-selective OAMs and pumping with elliptically polarized FWs simultaneously with tunable intensity contrast and time delay.[51,52]

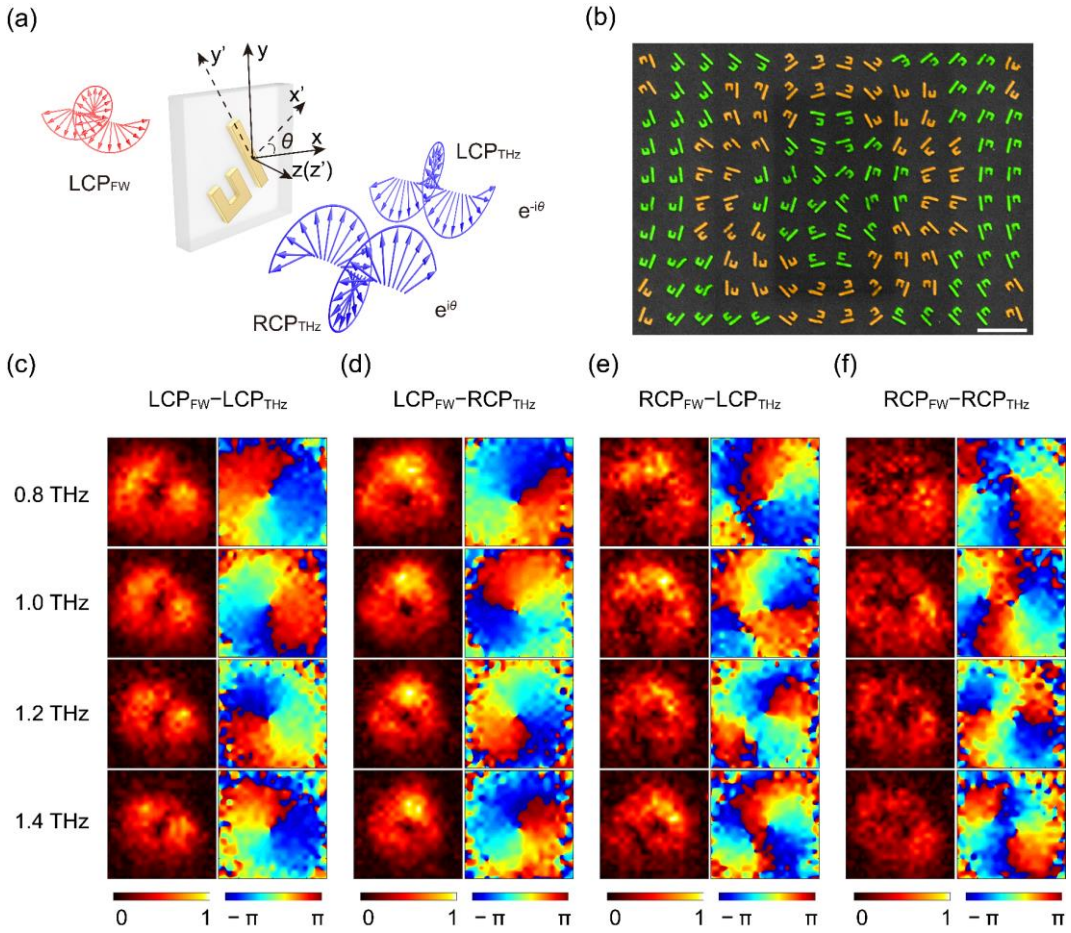

Figure 4. Handedness-selective nonlinear spin-orbital interaction for THz generation. a) Mechanism of the nonlinear PB phase for THz generation. b) Partial SEM image of the fabricated sample composed of left-handed (green) and right-handed (orange) chiral meta-molecules with ΔS = 70 nm (scale bar: 1000 nm). Going counter-clockwise around the center, the meta-molecule orientations rotate by −2π and +4π, respectively. c-f) Measured transverse amplitude (left) and phase (right) distributions of the generated LCP and RCP THz beams at 0.8, 1.0, 1.2, and 1.4 THz (top to bottom) under LCP and RCP FW pump.

3. Discussion

Conversion efficiency is an important indicator of a nonlinear THz source. Take the nonlinear metasurface composed of achiral meta-molecules with ΔS = 130 nm as a reference, the measured results under the *y*-polarized FW pump at 1280 nm show that the corresponding amplitude of the THz emission is 16% of that from a 200 μm-thick ZnTe crystal under 800 nm FW pump. Such a ratio is in a similar level as compared with the previous studies.[27-30] Considering the reported conversion efficiency of ZnTe,[53] the conversion efficiency here is

estimated to be 0.9×10^{-8} at 101.9 μJ cm^{-2} pump fluence, corresponding to a THz intensity of 2.3×10^{-9} μJ at the nonlinear metasurface plane. However, it should be mentioned that the thickness of the nonlinear metasurface here is only 48 nm. Taking the thickness into account, the effective conversion efficiency is greatly enhanced. Detail information can be seen in Figure S7.

Besides nonlinear PB phase control, our coupling-based designs also provide a robust route for achieving continuous and broadband control over the amplitude of the THz emission. For example, these meta-molecules under certain polarized pumps may be arranged on an interface to form amplitude distributions of gratings, zone plates and holograms. Moreover, the NLCD control in the chiral meta-molecules also implies an amplitude tuning ability of the THz generation under certain circularly polarized pumps. It can be combined with the nonlinear PB phase for achieving simultaneous control over amplitude and phase of the emitted THz waves, which can be further applied for generating more complex and high-quality THz wavefronts. In particular, pump-polarization-selective THz generation can in principle be engineered for any chosen pump polarization. More importantly, our results show that the above nonlinear control can be guided by simply observing the linear responses of the meta-molecules, i.e., the resonance strength of the MDR, which can greatly simplify the design processes.

As for the handedness-selective generator-manipulators, we show that they can combine the functionalities of two different THz field controls and THz generation in a single device. This can further broaden the applications of nonlinear metasurfaces. In terms of the proposed one for THz vortex beam generations of different OAMs, it can be potential in future multi-channel THz communication applications, where different modulating signals to the LCP and RCP FW pumps can be respectively transferred to the generated THz vortex beams with $l = \pm 1$ and $l = \pm 2$, and then let the THz waves pass the information in the wireless part. Interestingly, when the deivce is pumped from the back side, the NLCD and the nonlinear PB phase in each chiral meta-molecule will reverse accordingly. Therefore, the device will generate LCP and

RCP THz vortex beams with OAMs of $l = 2$ and -2 under LCP FW pump, while the RCP FW pump will generate LCP and RCP THz vortex beams with OAMs of $l = -1$ and 1. It is worth mentioning that, the THz vortex beam generation here is based on nonlinear PB phase method, which is designed only for nonlinear process. This implies that similar controlling ways can hardly be extended to other conventional THz generation schemes. Though nanostructures made from nonlinear crystal film may be one route, however, if the relations between the crystal orientation and the structure orientations cannot be fixed, it may bring varying nonlinear responses in different structures.

While the coupling strength between meta-atoms in our meta-molecules was fixed at the time of fabrication, it can be combined with nanomechanical photonic metamaterial[54] (e.g. based on NEMS) technique, which offers a route to dynamic control over such a coupling. Nanomechanical THz generator-manipulators could in principle switch the nonlinear THz emission on and off or offer dynamic control over pump-handedness-selectivity. Compared to MEMS THz metamaterials,[55-57] the much smaller characteristic dimensions of photonic metamaterial nonlinear THz generators imply that the moving parts can be orders of magnitude smaller, lighter and therefore faster. Nanomechanical photonic metamaterials with fundamental mechanical resonances at up to 150 MHz have been reported[58] (though ≈1 MHz is more typical), implying that sub-microsecond response times should be feasible. This indicates an opportunity to develop fast THz modulators.

4. Conclusion

A coupling method capable of controlling broadband terahertz emission in nonlinear metasurfaces is experimentally demonstrated, leading to 93.8% amplitude modulation depth (achiral meta-molecules) and NLCD manipulation with near unity regulating range (chiral meta-molecules). In particular, utilizing the chiral meta-molecules with handedness-selective features, we show experimentally that they enable the generation of two independent THz field

distributions revealed by LCP and RCP pumps, in a single device of nanoscale thickness. It acts as a handedness-selective THz vortex/vector beam generator. Comparing to its counterparts based on linear THz metasurfaces, the device footprint here is much more compact, benefitting from the smaller phase controlling resolution of the meta-molecule, and it does not require any existing THz source. Meanwhile, our method demonstrates how coupling provides a useful degree of freedom in engineering nonlinear THz generation and manipulation in metasurfaces and opens a gateway towards functional and multi-functional nonlinear THz photonic devices. Moreover, the use of coupling effect in control of a nonlinear process, and engineering of meta-molecules that exhibit this process for only one of two orthogonal pump polarizations, are not necessarily limited to THz generation, but may also be applicable to other nonlinear processes. For example, second-harmonic generation (SHG), which is also a second-order nonlinear effect and possesses similar polarization and efficiency dependence to the MDR in SRR.[59-60]

5. Experimental Section

Sample fabrication: The nonlinear metasurfaces are fabricated by a sequential process of electron beam lithography (EBL), electron beam evaporation and lift-off. First, the metasurface patterns are created using a JEOL 9300FS 100 kV EBL tool. Next, 3 nm Ti and 40 nm Au films are successively deposited using e-beam evaporation. At last, lift-off and cleaning processes are performed to obtain the metasurfaces. All the samples are fabricated on a 5 nm ITO-coated fused quartz substrate of 0.7 mm thickness, where the thin ITO layer can not only prevent local charge accumulation during lithography, but also greatly enhance the THz generations in combination with plasmonic resonators.[29,43] This can help make it easier to observe the coupling controlled THz generation behaviors here.

Linear transmission measurement: The linear transmission spectra of all samples are measured using a custom-built infrared microscope. Near-infrared light emitted from a stabilized tungsten

infrared light source (Thorlabs, SLS202L/M) passes through a linear polarizer and is then focused onto the metasurface by an objective lens. The transmitted light is guided and collimated into a spectrometer (Princeton Instruments, Acton SpectraPro SP-2300). The reference spectrum is the transmitted light from an un-patterned area on the same substrate.

Nonlinear measurement: All the nonlinear measurements are performed using a custom-built THz time-domain spectroscopy (TDS) system, see **Figure 5**. It is pumped by a Ti: sapphire femtosecond laser amplifier (Coherent, Legend Elite Duo) with central wavelength of 800 nm, pulse duration of 35 fs, and a repetition rate of 1.0 kHz. The laser light is split into two beams by a beam splitter (BS). One is guided to a 1-mm-thickness 110-cut ZnTe crystal after passing through a beam expander composed by two lenses (L1 and L2), serving as the probe beam. The other is injected into an optical parameter amplifier (OPA, Coherent OperA Solo) to generate a near-infrared femtosecond laser beam, which serves as the pump beam with pulse duration of 65 fs. The central wavelength of the pump beam can be continuously tuned from 1160 nm to 2000 nm. To control the pump polarization, a half-wave plate (HWP), a linear polarizer (P1) and a super achromatic quarter-wave plate (SQWP) are inserted before the sample. The emitted THz wave is collected and focused by two parabolic mirrors (PM1 and PM2) with 2- and 4-inches focal lengths, respectively. Two THz linear polarizers P2 and P3 are inserted between them to measure the THz polarization components, in which P3 is fixed to allow transmission of only the horizontally polarized component while P2 is rotated to allow transmission of either −45° or 45° polarized components. After passing through a polished 2-mm-thickness silicon wafer, the THz beam is collinear with the reflected optical probe beams, which are then incident onto the ZnTe crystal. Based on the electro-optical effect, the polarization state of the probe beam will be modulated by the transient THz electric field, which changes form linearly polarized to slightly elliptically polarized. By shining the transmitted probe beam onto an iris, a quarter-wave plate (QWP) and a Wollaston prism (WP) in sequence, the transient THz field,

which is proportional to the intensity difference between the two orthogonally polarized beams from the WP, can be extracted using a balance detection (BD) technique. At last, by gradually controlling the time delay between the probe beam and the THz pulse through scanning the delay line, the time-domain THz waveform is retrieved. To measure the transverse field distributions of the THz beam, the ZnTe crystal and the iris are mounted on a motorized two-dimensional translation stage and raster scanned in the *x*-*y* plane.

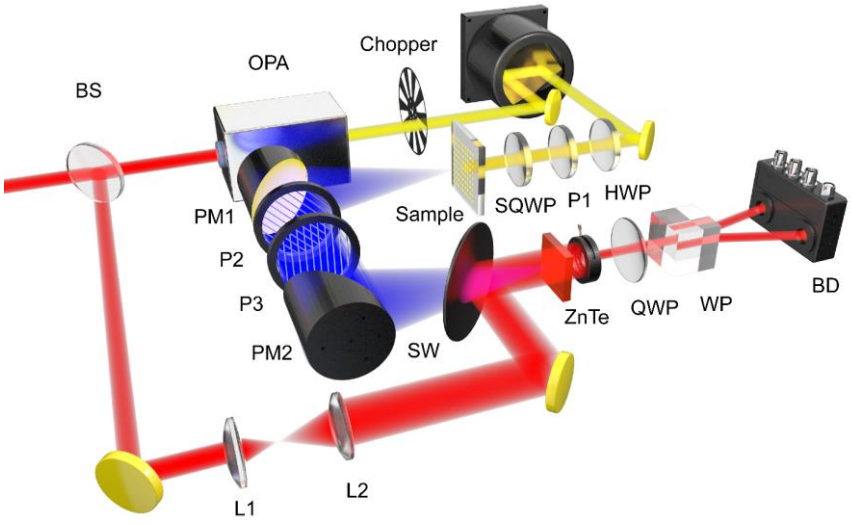

Figure 5. Schematic of the experimental setup. BS: beam splitter; OPA: optical parameter amplifier; L: lens; P: linear polarizer; HWP: half-wave plate; QWP: quarter-wave plate; SQWP: super achromatic quarter-wave plate; PM: parabolic mirror; SW: silicon wafer; WP: Wollaston prism; BD: balanced detector.

Statistical Analysis: All data were analyzed using MATLAB (MathWorks). The presented experimental results on THz generations, including THz time-domain signals and field distributions, are averaged from three-times measurements to improve the signal-to-noise ratio. Taking the THz time-domain signal from the achiral meta-molecule with ΔS = 130 nm as an example (see Figure 2e), the signal-to-noise ratio is about 179.

Supporting Information

Supporting Information is available from the Wiley Online Library or from the author.

Conflict of Interest

The authors declare no conflict of interest.

Acknowledgements

This work is supported by the National Natural Science Foundation of China (Grant Nos. 61735012, 62025504, 62075158, 61875150, 61935015, 62005193, 11974259, 62271004, 62231003 and U20A20164); the UK's Engineering and Physical Sciences Research Council (Grant No. EP/T02643X/1); H2020 ERC Consolidator Grant (648783). Following a period of embargo, the data from this paper will be available from the University of Southampton ePrints research repository: https://doi.org/10.5258/SOTON/D2310

Received:
Revised:
Published online:

References

[1] T. Nagatsuma, G. Ducournau, C. C. Renaud, *Nat. Photonics* **2016**, 10, 371.

[2] T. Kleine-Ostmann, T. Nagatsuma, *J. Infrared Millim. Terahertz Waves* **2011**, 32, 143.

[3] M. Beruete, I. Jáuregui-López, *Adv. Opt. Mater.* **2020**, 8, 1900721.

[4] W. L. Chan, J. Deibel, D. M. Mittleman, *Rep. Prog. Phys.* **2007**, 70, 1325.

[5] A. Dobroiu, C. Otani, K. Kawase, *Measurement Science and Technology* **2006**, 17, R161.

[6] D. R. Bacon, J. Madeo, K. M. Dani, *J. Opt.* **2021**, 23, 064001.

[7] J. Hebling, K. L. Yeh, M. C. Hoffmann, K. A. Nelson, *IEEE J. Sel. Top. Quantum Electron.* **2008**, 14, 345.

[8] X. Xie, J. Dai, X. C. Zhang, *Phys. Rev. Lett.* **2006**, 96, 075005.

[9] L. Huang, Y. Zhou, H. Qiu, H. Bai, C. Chen, W. Yu, L. Liao, T. Guo, F. Pan, B. Jin, C. Song, *Adv. Mater.* **2022**, 34, 2205988.

[10] X. Wu, H. Wang, H. Liu, Y. Wang, X. Chen, P. Chen, P. Li, X. Han, J. Miao, H. Yu, C. Wan, J. Zhao, S. Chen, *Adv. Mater.* **2022**, 34, 2204373.

[11] H. Qiu, L. Zhou, C. Zhang, J. Wu, Y. Tian, S. Cheng, S. Mi, H. Zhao, Q. Zhang, D. Wu, B. Jin, J. Chen, P. Wu, *Nat. Phys.* **2021**, 17, 388.

[12] T. Seifert, S. Jaiswal, U. Martens, J. Hannegan, L. Braun, P. Maldonado, F. Freimuth, A. Kronenberg, J. Henrizi, I. Radu, E. Beaurepaire, Y. Mokrousov, P. M. Oppeneer, M. Jourdan, G. Jakob, D. Turchinovich, L. M. Hayden, M. Wolf, M. Münzenberg, M. Kläui, T. Kampfrath, *Nat. Photonics* **2016**, 10, 483.

[13] Z. Tan, F. Fan, S. Guan, H. Wang, D. Zhao, Y. Ji, S. Chang, *Adv. Sci.* **2023**, 10, 2204916.

[14] H.-J. Zhao, F. Fan, T.-R. Zhang, Y.-Y. Ji, S.-J. Chang, *Photonics Res.* **2022**, 10, 1097.

[15] F. Fan, D. Zhao, Z. Tan, Y. Ji, J. Cheng, S. Chang, *Adv. Opt. Mater.* **2021**, 9, 2101097.

[16] H.-J. Zhao, F. Fan, Y.-Y. Ji, S.-L. Jiang, Z.-Y. Tan, S.-J. Chang, *Photonics Res.* **2022**, 10, 2658.

[17] L. Niu, Q. Xu, X. Zhang, Z. Zhang, S. Li, X. Chen, Y. Xu, J. Ma, M. Kang, J. Han, W. Zhang, *ACS Appl. Mater. Interfaces* **2021**, 13, 5844.

[18] L. Liu, X. Zhang, M. Kenney, X. Su, N. Xu, C. Ouyang, Y. Shi, J. Han, W. Zhang, S. Zhang, *Adv. Mater.* **2014**, 26, 5031.

[19] C. Zheng, G. Wang, J. Li, J. Li, S. Wang, H. Zhao, M. Li, Z. Yue, Y. Zhang, Y. Zhang, J. Yao, *Adv. Opt. Mater.* **2021**, 9, 2002007.

[20] Y. Xu, H. Zhang, Q. Li, X. Zhang, Q. Xu, W. Zhang, C. Hu, X. Zhang, J. Han, W. Zhang, *Nanophotonics* **2020**, 9, 3393.

[21] T. Wu, Q. Xu, X. Zhang, Y. Xu, X. Chen, X. Feng, L. Niu, F. Huang, J. Han, W. Zhang, *Adv. Sci.* **2022**, 9, 2204664.

[22] T. Wu, X. Zhang, Q. Xu, E. Plum, K. Chen, Y. Xu, Y. Lu, H. Zhang, Z. Zhang, X. Chen, G. Ren, L. Niu, Z. Tian, J. Han, W. Zhang, *Adv. Opt. Mater.* **2022**, 10, 2101223.

[23] B. Chen, J. Wu, W. Li, C. Zhang, K. Fan, Q. Xue, Y. Chi, Q. Wen, B. Jin, J. Chen, P. Wu, *Laser Photonics Rev.* **2022**, 16, 2100472.

[24] B. Chen, X. Wang, W. Li, C. Li, Z. Wang, H. Guo, J. Wu, K. Fan, C. Zhang, Y. He, B. Jin, J. Chen, P. Wu, *Sci. Adv.* **2022**, 8, eadd1296.

[25] A. Krasnok, M. Tymchenko, A. Alù, *Mater. Today* **2018**, 21, 8.

[26] G. Li, S. Zhang, T. Zentgraf, *Nat. Rev. Mater.* **2017**, 2, 17010.

[27] L. Luo, I. Chatzakis, J. Wang, F. B. P. Niesler, M. Wegener, T. Koschny, C. M. Soukoulis, *Nat. Commun.* **2014**, 5, 3055.

[28] C. McDonnell, J. Deng, S. Sideris, T. Ellenbogen, G. Li, *Nat. Commun.* **2021**, 12, 30.

[29] Y. Lu, X. Feng, Q. Wang, X. Zhang, M. Fang, W. E. I. Sha, Z. Huang, Q. Xu, L. Niu, X. Chen, C. Ouyang, Y. Yang, X. Zhang, E. Plum, S. Zhang, J. Han, W. Zhang, *Nano Lett.* **2021**, 21, 7699.

[30] C. McDonnell, J. Deng, S. Sideris, G. Li, T. Ellenbogen, *Nano Lett.* **2022**, 22, 2603.

[31] E. Minerbi, S. Keren-Zur, T. Ellenbogen, *Nano Lett.* **2019**, 19, 6072.

[32] A. Zdagkas, C. McDonnell, J. Deng, Y. Shen, G. Li, T. Ellenbogen, N. Papasimakis, N. I. Zheludev, *Nat. Photonics* **2022**, 16, 523.

[33] J. Gu, R. Singh, X. Liu, X. Zhang, Y. Ma, S. Zhang, S. A. Maier, Z. Tian, A. K. Azad, H.-T. Chen, A. J. Taylor, J. Han, W. Zhang, *Nat. Commun.* **2012**, 3, 1151.

[34] N. Liu, L. Langguth, T. Weiss, J. Kästel, M. Fleischhauer, T. Pfau, H. Giessen, *Nat. Mater.* **2009**, 8, 758.

[35] S. Zhang, D. A. Genov, Y. Wang, M. Liu, X. Zhang, *Phys. Rev. Lett.* **2008**, 101, 047401.

[36] S. Li, X. Zhang, Q. Xu, M. Liu, M. Kang, J. Han, W. Zhang, *Opt. Express* **2020**, 28, 20083.

[37] M. Lawrence, N. Xu, X. Zhang, L. Cong, J. Han, W. Zhang, S. Zhang, *Phys. Rev. Lett.* **2014**, 113, 093901.

[38] M. Manjappa, Y. K. Srivastava, L. Cong, I. Al-Naib, R. Singh, *Adv. Mater.* **2017**, 29, 1603355.

[39] B. Luk'yanchuk, N. I. Zheludev, S. A. Maier, N. J. Halas, P. Nordlander, H. Giessen, C. T. Chong, *Nat. Mater.* **2010**, 9, 707.

[40] I. Romero, J. Aizpurua, G. W. Bryant, F. J. G. d. Abajo, *Opt. Express* **2006**, 14, 9988.

[41] X. Liu, J. Gu, R. Singh, Y. Ma, J. Zhu, Z. Tian, M. He, J. Han, W. Zhang, *Appl. Phys. Lett.* **2012**, 100, 131101.

[42] M. Fang, K. Niu, Z. Huang, W. E. I. Sha, X. Wu, T. Koschny, C. M. Soukoulis, *Opt. Express* **2018**, 26, 14241.

[43] E. Minerbi, S. Sideris, J. B. Khurgin, T. Ellenbogen, *Nano Lett.* **2022**, 22, 6194.

[44] W. Jia, M. Liu, Y. Lu, X. Feng, Q. Wang, X. Zhang, Y. Ni, F. Hu, M. Gong, X. Xu, Y. Huang, W. Zhang, Y. Yang, J. Han, *Light: Sci. Appl.* **2021**, 10, 11.

[45] A. Block, M. Liebel, R. Yu, M. Spector, Y. Sivan, F. J. García de Abajo, N. F. van Hulst, *Sci. Adv.* **2019**, 5, eaav8965.

[46] Q. Wang, E. Plum, Q. Yang, X. Zhang, Q. Xu, Y. Xu, J. Han, W. Zhang, *Light: Sci. Appl.* **2018**, 7, 25.

[47] S. Chen, F. Zeuner, M. Weismann, B. Reineke, G. Li, V. K. Valev, K. W. Cheah, N. C. Panoiu, T. Zentgraf, S. Zhang, *Adv. Mater.* **2016**, 28, 2992.

[48] E. Plum, V. A. Fedotov, N. I. Zheludev, *Appl. Phys. Lett.* **2009**, 94, 131901.

[49] V. A. Fedotov, P. L. Mladyonov, S. L. Prosvirnin, A. V. Rogacheva, Y. Chen, N. I. Zheludev, *Phys. Rev. Lett.* **2006**, 97, 167401.

[50] G. Li, S. Chen, N. Pholchai, B. Reineke, P. W. H. Wong, Edwin Y. B. Pun, K. W. Cheah, T. Zentgraf, S. Zhang, *Nat. Mater.* **2015**, 14, 607.

[51] M. Liu, P. Huo, W. Zhu, C. Zhang, S. Zhang, M. Song, S. Zhang, Q. Zhou, L. Chen, H. J. Lezec, A. Agrawal, Y. Lu, T. Xu, *Nat. Commun.* **2021**, 12, 2230.

[52] Z. H. Jiang, L. Kang, T. Yue, H.-X. Xu, Y. Yang, Z. Jin, C. Yu, W. Hong, D. H. Werner, C.-W. Qiu, *Adv. Mater.* **2020**, 32, 1903983.

[53] F. Blanchard, L. Razzari, H. C. Bandulet, G. Sharma, R. Morandotti, J. C. Kieffer, T. Ozaki, M. Reid, H. F. Tiedje, H. K. Haugen, F. A. Hegmann, *Opt. Express* **2007**, 15, 13212.

[54] N. I. Zheludev, E. Plum, *Nat. Nanotechnol.* **2016**, 11, 16.

[55] M. Manjappa, P. Pitchappa, N. Singh, N. Wang, N. I. Zheludev, C. Lee, R. Singh, *Nat. Commun.* **2018**, 9, 4056.

[56] W. M. Zhu, A. Q. Liu, T. Bourouina, D. P. Tsai, J. H. Teng, X. H. Zhang, G. Q. Lo, D. L. Kwong, N. I. Zheludev, *Nat. Commun.* **2012**, 3, 1274.

[57] W. M. Zhu, A. Q. Liu, X. M. Zhang, D. P. Tsai, T. Bourouina, J. H. Teng, X. H. Zhang, H. C. Guo, H. Tanoto, T. Mei, G. Q. Lo, D. L. Kwong, *Adv. Mater.* **2011**, 23, 1792.

[58] A. Karvounis, J.-Y. Ou, W. Wu, K. F. MacDonald, N. I. Zheludev, *Appl. Phys. Lett.* **2015**, 107, 191110.

[59] M. W. Klein, M. Wegener, N. Feth, S. Linden, *Opt. Express* **2007**, 15, 5238.

[60] M. W. Klein, C. Enkrich, M. Wegener, S. Linden, *Science* **2006**, 313, 502.